

Cite this: *Mater. Adv.*, 2023,
4, 1389

Evidence of progressive Fe²⁺ to Fe³⁺ oxidation in Fe²⁺-doped ZnO nanoparticles

F. F. H. Aragón, *^{ab} L. Villegas-Lelovsky, ^{cf} J. G. Parizaka,^a E. G. Zela,^a
R. Bendezu,^a R. O. Gallegos, ^a D. G. Pacheco-Salazar, ^a S. W. da Silva, ^b
R. Cohen, ^d L. C. C. M. Nagamine, ^d J. A. H. Coaquira ^b and P. C. Morais ^{be}

Oxide-diluted magnetic semiconductors have received considerable attention in diverse scientific and technological fields because they combine the optoelectronic properties of the hosting semiconductor with the magnetic properties of the metal dopant. In this report, the role of Fe doping on the structural, vibrational, optical, hyperfine, and magnetic properties of Fe-doped ZnO nanoparticles (Zn_{1-x}Fe_xO) synthesized *via* a polymeric precursor method is presented. Our findings display that the crystallite size decreases from ~23 nm ($x = 0.000$) to ~8 nm ($x = 0.200$) as the Fe-content (x) is increased. From the XRD data analysis, our results suggest an isovalent solid solution between Fe²⁺ and Zn²⁺ ions for lower Fe-content (up to 0.075) and aliovalent solution (Fe³⁺ and Zn²⁺ ions) for higher Fe-content. Elliot's theory was used to assess the band gap energy of $E_g \sim 3.4$ eV, and an exciton binding energy of $E_b \sim 66$ meV for the undoped sample. The excitonic peak exhibits a broadening trend with increasing Fe-content, suggesting disorder enhancement in the ZnO matrix. Besides, FTIR data analysis suggests that the Zn–O bond length increases with Fe-content up to 0.075 and decreases above this value. The intensity ratio of the O–H and Zn–O modes shows a discontinuity as the Fe-content is increased. Room temperature Mössbauer spectra carried out for samples with $x = 0.050$, 0.075, and 0.200 show that the isomer shift and quadrupole splitting increase with the Fe-content, in agreement with the structural properties. Magnetic measurements suggest that the iron ions stabilize as Fe²⁺ in samples with low Fe-content and then as Fe³⁺ in samples with high Fe-content. Besides, the occurrence of short-range antiferromagnetic interactions was determined, which becomes stronger as the Fe-content is increased.

Received 29th January 2023,
Accepted 5th February 2023

DOI: 10.1039/d3ma00053b

rsc.li/materials-advances

1. Introduction

Diluted magnetic oxide semiconductor (DMOS) has received considerable attention because it combines the optoelectronic properties of semiconductors (oxide semiconductors) with the magnetic properties of transition metals. In this regard, ZnO undoped and doped with transition metal ions (such as Fe, Ni, Co among others) and rare-earth ions (such as Ce, Er, Gd among others) have been used for several applications. Moreover, a wide range of methods have been used to produce Fe-doped ZnO nanostructures, among which we can point out

solution combustion,¹ sol-gel,² and hydrothermal.³ The polymeric precursor method (Pechine's method) used in the present study, in addition to being a bottom-up synthesis route, is a highly reproducible approach, which is based on the formation of chelate between mixed cations and citric acid. The metal ions are chelated, and these chelates are then cross-linked with ethylene glycol to form a gel by esterification. After thermal treatment in the air (~400 °C), a removal of all organic substances is accomplished. Subsequently, thermal annealing at high temperatures (> 400 °C) improves the crystallinity of the as-synthesized nanoparticles.⁴ However, due to the high temperatures employed in this chemical route, while compared with other methods (such as hydrothermal and precipitation) the polymeric precursor method suffers from a lack of morphology control. Regarding their applications, one can highlight their use in wastewater treatment processes. In this scenario, Andia-Huaracha *et al.*, reported the photocatalytic activity (PCA) of ZnO nanoparticles (NPs) synthesized *via* the polymeric precursor method and presenting mean crystallite size in the range of 23–150 nm.⁵ Moreover, the PCA tests of the ZnO NPs do not show a straightforward dependence on the NPs' size,

^a Universidad Nacional de San Agustín de Arequipa, Av Independencia SN, Arequipa, Peru. E-mail: ffharagon@gmail.com^b University of Brasília, Institute of Physics, Brasília, DF 70919-970, Brazil^c Departamento de Física, Centro de Ciências Exatas e de Tecnologia, Universidade Federal de São Carlos, São Carlos, SP 13565-905, Brazil^d Instituto de Física, Universidade de São Paulo, São Paulo, SP 05508-090, Brazil^e Catholic University of Brasília, Genomic Sciences and Biotechnology, Brasília, DF 71966-700, Brazil^f Physics Department, IGCE, Paulista State University, CEP 13506-900, Rio Claro, SP, Brazil

but it seems to be correlated with the density of defects.⁵ In addition, Rokhsat *et al.* reported the PCA of Fe-doped ZnO nanosheets on the *p*-nitrophenol degradation under visible light, revealing the high performance of the Fe-doped sample compared to the undoped one.³ On the other hand, based on the Langmuir isotherm analysis, ZnO nanocrystals decorated with regenerated microfibrillated cellulose scaffolds and containing 41 wt% ZnO were found to be very efficient in removing As(V) from water with a maximum capacity of 4.421 mg g⁻¹, at neutral pH (7).⁶

Importantly, in Fe-doped oxides, iron ions can exist in two regular oxidation states (Fe²⁺ and Fe³⁺), which could impact

differently the structural properties of the hosting ZnO nanocrystal due to differences in their ionic radii. The latter may be strongly reflected in the physicochemical properties of the Fe-doped ZnO structure. As a result, determining the oxidation state of heterovalent elements (such as Fe) is critical for understanding how the doped system works. Importantly, the oxidation state of iron ions in Fe-doped ZnO can be strongly dependent on the synthesis process.⁷ However, several reports show that iron is usually found as high spin Fe²⁺-ions substituting Zn²⁺-ions.⁷⁻⁹ It is noteworthy the report of George *et al.* regarding the study of Fe-doped ZnO NPs, suggesting that the



F. F. H. Aragón

Fermin F. H. Aragón received his PhD degree from the University of Brasilia (2013), Brazil. He was a postdoctoral fellow at the Center for the Development of Nuclear Technology (CDTN) and Visiting Professor at the Physics Institute of the University of Brasilia, Brazil (2016–2019), Research fellow at the Center for Biomedical Research (CBR) of the Population Council located at Rockefeller University, New York (2020). Associate Researcher at the Pon-

tifical Catholic University of Peru (PUCP), Associate Researcher at the National University of San Agustín of Arequipa (UNSA), Peru (2022). His research work mainly focuses on the production and studying of the structural, optical, electrical, hyperfine, and magnetic properties of nanomaterials, with technological applications such as gas sensors, photocatalysis, wastewater treatment process, and biomaterials for health applications.



L. Villegas-Lelovsky

Leonardo Villegas-Lelovsky received his PhD in Physical Sciences from the Center for Research and Advanced Studies (CINVESTAV-IPN), Mexico (2003). He was a postdoctoral fellow at the University of São Paulo, Brazil (2005) and Visiting Professor at the Physics Institute of the University of Brasilia, Brazil (2012). He is currently a researcher at the Paulista State University (UNESP) and a collaborator at the Federal

University of São Carlos (UFSCAR), Brazil. He has experience in Condensed Matter Physics, with an emphasis on simulation of electronic, optical, magnetic, and transport properties in nanostructured semiconductor systems and 2D graphene-like devices.



R. O. Gallegos

Raúl Omar Gallegos Jara received his Chemical Engineer Bachelor's degree at the National University of San Agustín of Arequipa, Peru. PhD in Environmental Sciences by the National University of San Agustín of Arequipa, Peru. He is the main professor in the Professional School of Chemical Engineering at the National University of San Agustín of Arequipa, Peru (since 1992). He has been the leader of the project

“Effect of the variables of formation of nanoparticles of zinc oxide with support in zeolite and its efficiency of removal of arsenic in waters of the province of Islay-Arequipa-Peru”, resulting in the present study. His research work mainly focuses on the use of new materials in wastewater treatment process applications.



D. G. Pacheco-Salazar

David G. Pacheco Salazar received his PhD from the University of São Paulo, Brazil (2004), in the area of Physics of Materials. He is currently Professor and Researcher of the National University of San Agustín of Arequipa (UNSA), Perú. Head of the Thin Films and Nanomaterials Laboratory of the UNSA, Associate Researcher at the Pontifical Catholic University of Peru (PUCP). He is currently doing research on thin film deposition by

sputtering technique and/or thermal evaporation, synthesis of nanoparticles by chemical routes, and their structural, optical, electrical, hyperfine, and magnetic properties characterizations aiming their use in environmental pollution and health applications.



entry of isovalent Fe^{2+} replacing Zn^{2+} leads to minimally distorted ZnO lattice structure.⁹ Determination of the iron oxidation state and the impact on the Fe-doped crystalline environment can be performed by different experimental techniques, such as X-ray photoelectron spectroscopy (XPS), X-ray absorption near-edge structure (XANES), inner-shell electron energy-loss spectroscopy (ISEELS), and Mössbauer

spectroscopy.^{8,10,11} The hyperfine parameters obtained from Mössbauer spectroscopy are commonly used to assess the oxidation state of iron in iron oxides. It is commonly known that the isomershift (IS) of Fe^{3+} in pure oxides is around 0.25 mm s^{-1} and 0.29 mm s^{-1} for the upper limit in tetrahedral coordination and lower limit for octahedral coordination, respectively. These values are lower than those expected for



S. W. da Silva

Sebastião William da Silva received his PhD from the Federal University of São Carlos, Brazil (1995). He is Full Professor of Physics at the University of Brasília, Brazil. He focuses his research on the development of nanostructured materials for biomedical applications and environmental depollution. So far, he has published 130 research papers in peer-reviewed journals. Appeared in recent World Scientist and University Rankings 2023 of AD Scientific Index.



L. C. C. M. Nagamine

Luiz C. C. M. Nagamine received his PhD degree in Physics from University of São Paulo, Brazil (1995), studying spin reorientation in RFe_{11}Ti and $\text{DyFe}_{11}\text{Ti}$. He held two years post-doc at the Centre D'Energie Atomique, Grenoble, France (1996–1997) and almost two years post-doc at the Centro Brasileiro de Pesquisas-Físicas (CBPF), Rio de Janeiro, Brazil (1998–1999), studying magnetic thin films, exchange-bias phenomena and magnetoresistance in spin valves. He has worked for nine years as Assistant Professor at the University Federal of Rio Grande do Sul, Porto Alegre, Brazil (2000–2009), continuing his work in studying magnetic anisotropy of magnetic films by ferromagnetic resonance, Mössbauer spectroscopy and magnetic characterizations. Since 2009, he has worked as Assistant Professor at the Institute of Physics, University of São Paulo, Brazil, growing magnetic nanoparticles by chemical synthesis and magnetic and morphological characterizations.



J. A. H. Coaquira

Jose A. Huamani Coaquira received his bachelor's degree in Physics from the National University of San Agustín of Arequipa, Peru (1991), PhD in Physics from the University of São Paulo, Brazil (1998). Postdoctoral fellow at the University of São Paulo (1998–2002), Brazil and University of Houston, USA (2003–2005). Currently, he works as Associate Professor at the University of Brasília. He has experience in

the field of condensed matter physics, with emphasis on magnetic materials and magnetic properties, working mainly on the following topics: production and characterization of hydrogen absorbing nanostructured intermetallic alloys, nanostructured magnetic semiconductors, and magnetic nanoparticles with potential applications in biotechnology and environmental protection.



P. C. Morais

Paulo Cesar de Morais was a Professor of Physics at the University of Brasília (UnB), Brazil (up to 2013), UnB's Emeritus Professor (2014), Visiting Professor at HUST, China (2012–2015), Distinguished Professor at AHU, China (2016–2019), Professor at the Catholic University of Brasília, Brazil (since 2018), CNPq-1A Fellowship since 2010. Senior Member of the IEEE Society, Academic Excellence Award from UnB (2012). Two-years post-doc with Bell Communications Research, USA (1987–1988); PhD in Solid State Physics from the Federal University of Minas Gerais (1986), Brazil; Graduated in Chemistry (1976) and in Physics (1977). Nearly 500 published papers in peer-reviewed journals plus 15 patents. Appeared in recent World ranking of top 1% scientists, such as 2020-Stanford and 2022-Research.com.



Fe^{2+} , which are in the range of 1.05–1.20 mm s^{-1} for octahedral coordination and in the range of 0.90–1.05 mm s^{-1} for tetrahedral coordination. The Mössbauer spectroscopy, however, is unusual and costly for most laboratories and, for this reason, new methods such as XRD and FTIR could be used instead.

In the present report, the structural, optical, vibrational, hyperfine and magnetic properties of Fe-doped ZnO nanoparticles are assessed aiming to determine the effect of iron-ions while entering in the ZnO hosting matrix. Moreover, one is interested in finding out how the oxidation state of iron-ions is modulated through the entry of iron in the ZnO hosting matrix.

2. Samples description and experimental details

Undoped and Fe-doped ZnO nanoparticles were synthesized by the polymer precursor chemical method using zinc nitrate hexahydrate ($\text{Zn}(\text{NO}_3)_2 \cdot 6\text{H}_2\text{O}$), iron nitrate nonahydrate ($\text{Fe}(\text{NO}_3)_3 \cdot 9\text{H}_2\text{O}$), ethylene glycol ($\text{C}_2\text{H}_4(\text{OH})_2$), and citric acid ($\text{C}_6\text{H}_8\text{O}_7$). To make the polymer precursor gel, the following steps were performed: citric acid (47.7%) and zinc nitrate hexahydrate (31.7%) were dissolved in ethylene glycol (20.6%) at 70 °C with magnetic stirring, then the temperature was raised to 120 °C to enhance citric acid and ethylene glycol polymerization. For iron doping, the amount of iron was controlled according to the atomic ratio $\text{Fe}/(\text{Fe} + \text{Zn})$, where x mol of iron (x mol of the iron nitrate nonahydrate) was mixed with $(1 - x) \times \text{Eff}$ mol of the ZnO resin, where Eff is the resin's efficiency. After promoting polymerization, the obtained liquid was pyrolyzed at 450 °C for 4 h. The final carbon-rich powder was thermally treated at 500 °C for 6 h. Homogeneous and energetically metastable powders were obtained. X-Ray diffraction (XRD) measurements at room temperature were performed using a Rigaku MiniFlex 600 X-ray diffractometer equipped with Cu $K\alpha$ radiation ($\lambda = 1.5418 \text{ \AA}$) and scanning in the 2θ range of 20°–80°. The instrumental contribution was removed using a Si standard sample. UV-Vis spectra were collected using a Shimadzu UV-1800 UV/Visible Scanning Spectrophotometer, in a range of measurement from 190 to 1100 nm. Fourier-transform infrared spectroscopy (FTIR) measurements were carried out (samples pressed in KBr pellet) using a Bruker VERTEX 70 FT-IR spectrometer, scanning in the wavenumber range of 450–4000 cm^{-1} . TEM images were performed with a JEOL microscope, model JEM-2100. Mössbauer measurements were carried out using a commercial spectrometer (WisselMössbauer spectrometer) equipped with a ^{57}Co source, operating in the constant acceleration mode and scanning the velocity in the range of $\pm 10 \text{ mm} \times \text{s}^{-1}$. Using the NORMOS software package, the Mössbauer spectra were curve fitted by minimizing the chi-square (χ^2) parameter. Magnetic measurements were performed using a commercial SQUID magnetometer (Quantum Design), in the temperature range of 2–300 K, and applied magnetic fields up to $\pm 70 \text{ kOe}$.

3. Results and discussions

Fig. 1(a) shows the XRD patterns of the undoped and Fe-doped ZnO nanoparticles ($\text{Zn}_{1-x}\text{Fe}_x\text{O}$, with x from 0.000 to 0.200). According to the XRD data, the wurtzite crystal structure is identified as the crystalline phase in all samples, in agreement with the Inorganic Crystal Structure Database (ICSD) card No. 34477. Within the XRD equipment's limit, no secondary phase was detected, indicating that the materials obtained through the employed chemical process are single-phase in the Fe-content (x) range of 0.000–0.200. Besides, a broadening of the XRD peaks is also detected, which can be correlated with a decrease in the mean crystallite size ($\langle D \rangle$) and/or an increase in residual strain ($\langle \epsilon \rangle$), which will be discussed later on in this report. It can also be seen that the (101) XRD peak has the highest intensity, indicating a high degree of crystallinity in the powder samples. To assess the structural parameters, the XRD patterns were analyzed using the Generalized Structure Analysis System (GSAS) software¹² modeling the peaks with Lorentzian shape functions. Fig. 2(b) shows a typical refinement for the undoped ($x = 0.000$) and Fe-doped ($x = 0.100, 0.200$) samples, where the cross symbol (+) represents experimental data, the solid red line represents the theoretical XRD curve, and the solid blue line at the bottom of the panels represents the difference between them. According to the refinement quality parameter ($S = R_{\text{Exp}}/R_{\text{Wp}}$, where the R -factors R_{Exp} and R_{Wp} quantify the quality of the refinement) all performed refinements ($S < 2$) are acceptable (see Table 1).

The lattice constants on the undoped ZnO NPs are $a = b = 3.2493 \pm 0.0001 \text{ \AA}$ and $c = 5.2070 \pm 0.0002 \text{ \AA}$. The extracted unit cell volume is $V = 47.611 \pm 0.004 \text{ \AA}^3$. These findings are in excellent agreement with the values of $a = b = 3.250 \text{ \AA}$, $c = 5.207 \text{ \AA}$, and $V = 47.63 \text{ \AA}^3$ reported in the literature.¹³ However, for Fe-doped ZnO NPs, interesting results are observed in regard to the unit cell volume (V), which displays an increasing trend as the Fe-content increases up to $x = 0.075$ (see Fig. 2(a)), followed by a decreasing tendency. Taking into account that within the ZnO matrix the Zn^{2+} -ions present four-fold coordination, that finding can be explained by two plausible scenarios. Firstly, at a lower Fe-content (up to $x = 0.075$), an entry of Fe^{2+} -ions with an ionic radius equal to 0.63 Å , which is greater than the ionic radius of Zn^{2+} (0.60 Å), explains the increase of the unit cell volume, as it is displayed in Fig. 2(a). This isovalent solid solution scenery is energetically more likely. Moreover, at higher Fe-content (above $x = 0.075$), the entry of trivalent iron-ions (Fe^{3+}) with an ionic radius equals to 0.49 Å (four-fold coordination),¹⁴ may lead to a decrease in the unit cell volume (V), as it is displayed in Fig. 2(a). As a result of the aforesaid, and taking into account what has been reported in the literature, doping ions segregate on the nanoparticle surface, and segregation increases as the doping content increases.¹⁵ Therefore, an alternative and feasible scenario can be built using Fe^{2+} -ions in the NP's core and Fe^{3+} -ions onto the NP's surface, in accordance with the result reported by McLeod *et al.*,¹⁶ claiming that Fe-doping in bulk ZnO promotes isovalent cation substitution ($\text{Fe}^{2+} \rightarrow \text{Zn}^{2+}$). Meanwhile, Fe-doping near the surface induces both isovalent ($\text{Fe}^{2+} \rightarrow \text{Zn}^{2+}$) and aniovalent substitution ($\text{Fe}^{3+} \rightarrow \text{Zn}^{2+}$).¹⁷ Also, this fact may



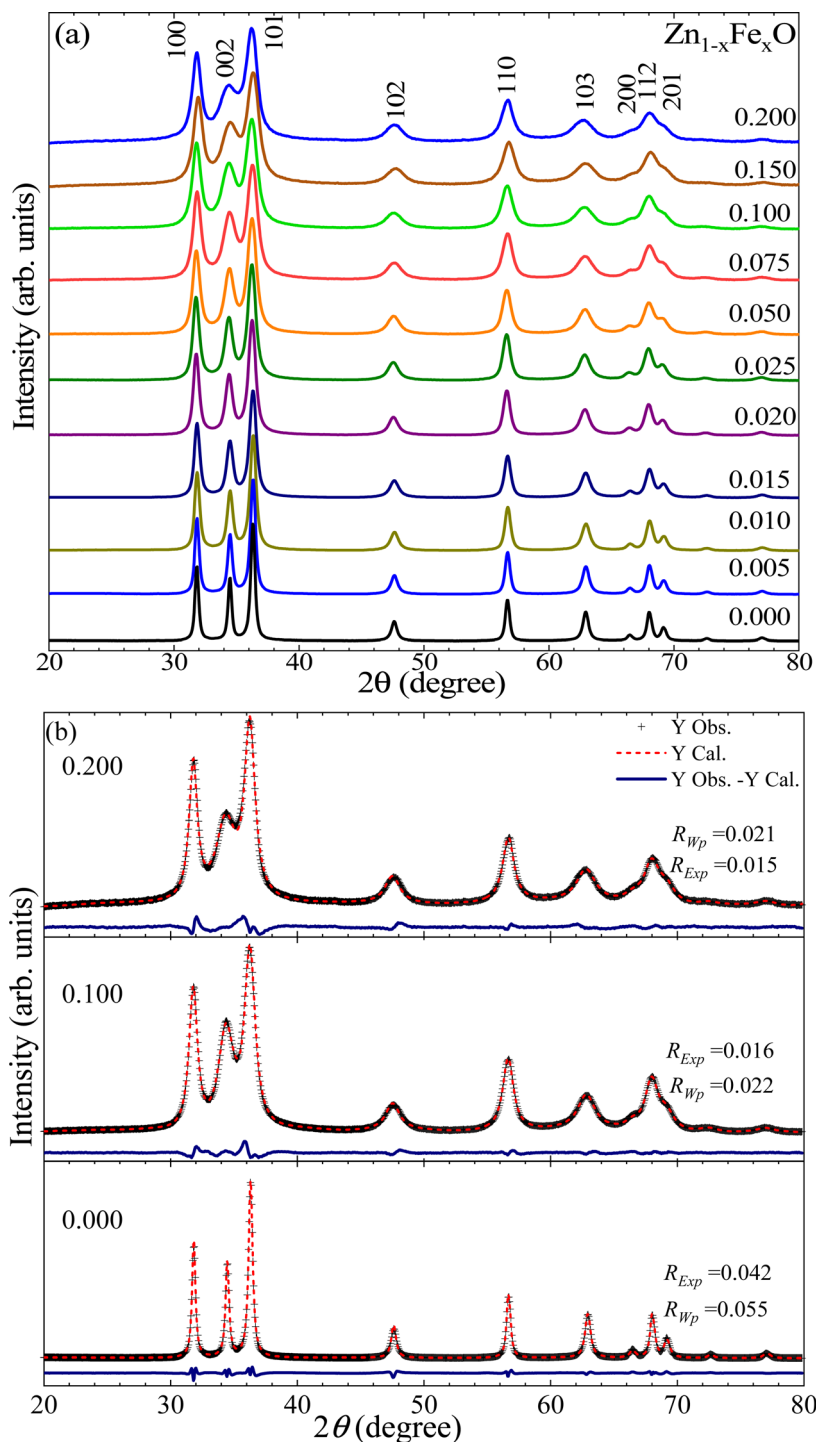


Fig. 1 (a) XRD of the $\text{Zn}_{1-x}\text{Fe}_x\text{O}$ NPs, with x varying from 0.000 to 0.200. (b) Rietveld refinement of the $x = 0.000$, 0.100, and 0.200. In (b) the cross symbols (+) represent experimental (observed) data, the dashed red line represents the calculated XRD curve, and the solid blue line (see at the bottom) shows the difference between them.

be related to the Kataoka *et al.* report, showing that Fe^{3+} -ions predominate onto the surface of NPs.¹⁶ A second possible scenario is related to the unit cell volume dependence (see Fig. 2(a)) on the ionic radius of both the Fe^{3+} -ion in six-fold coordination (0.65 Å) and in four-fold coordination (0.49 Å),¹⁴ respectively larger and smaller than the ionic radius of Zn^{2+} -ions

(0.60 Å). Within this second scenario, lower Fe-content (up to $x = 0.075$) favors the entry of Fe^{3+} -ions in six-fold coordination, whereas higher Fe-content (above $x = 0.075$) favors the entry of Fe^{3+} -ions in four-fold coordination, as represented by the data collected in Fig. 2(a). The second model picture could explain fairly well the observed experimental trends regarding the unit



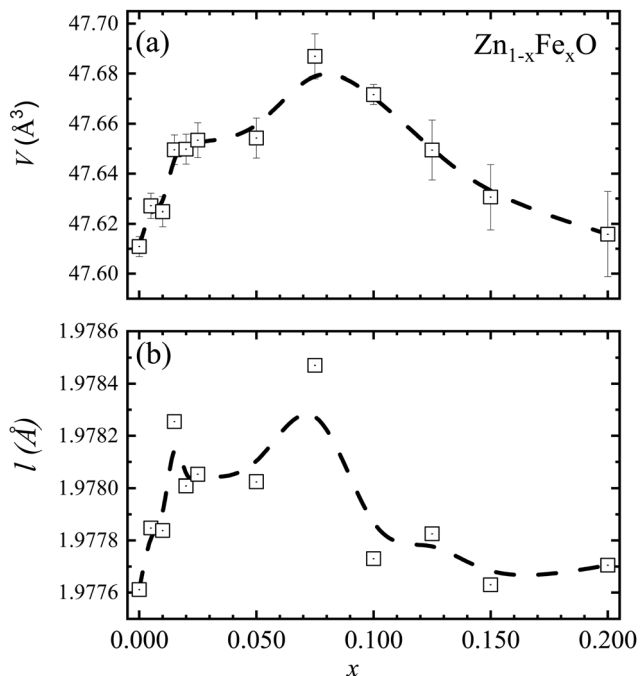


Fig. 2 (a) Unit cell volume (V). (b) Bond length (l) as a function of the Fe-content (x). Data obtained from the XRD analysis. Dashed lines are guides to the eye.

cell volume. However, the entry of iron-ions in positions other than the tetrahedral (four-fold coordination) is energetically more expensive, as this would imply iron-ions entering into interstitial positions (six-fold coordination), much more unlikely. Meanwhile, the entry of Fe^{3+} -ions into regions with a high degree of crystalline disorder (like the surface) plus the coexistence of $\text{Fe}^{3+}/\text{Fe}^{2+}$ became more likely as the Fe-content increases, as it is suggested in the literature.¹⁶ Fig. 1(b) displays the typical Rietveld refinement for $x = 0.000, 0.100$ and 0.200 in the $\text{Zn}_{1-x}\text{Fe}_x\text{O}$ NPs, where the symbol (+) represents the experimental data, the solid red line the calculated XRD pattern data, and in the bottom, the solid blue line the difference between them. Fig. 2(b) shows the bond length (l) as a function of Fe-content (x), which is consistent with the unit cell volume trend shown in Fig. 2(a). Regarding the density, the

Table 1 Lattice constants a , c , c/a crystallite size ($\langle D \rangle$) and density (ρ) were obtained through the Rietveld refinement. S represents the quantitative value displaying the refinement quality

Fe-content (x)	a (Å)	c (Å)	c/a	$\langle D \rangle$ (nm)	ρ (g cm^{-3})	S
0.000	3.2493(1)	5.2070(2)	1.6025	23.3	5.68	1.31
0.005	3.2496(1)	5.2078(2)	1.6026	19.8	5.67	1.30
0.010	3.2493(1)	5.2086(3)	1.6030	17.5	5.67	1.27
0.015	3.2499(1)	5.2101(3)	1.6031	15.0	5.66	1.27
0.020	3.2494(1)	5.2099(3)	1.6034	13.6	5.66	1.27
0.025	3.2493(2)	5.2104(4)	1.6035	13.5	5.66	1.27
0.050	3.2498(2)	5.2084(4)	1.6027	11.9	5.64	1.34
0.075	3.2494(3)	5.2135(5)	1.6044	10.2	5.62	1.35
0.100	3.2479(1)	5.2127(3)	1.6049	10.0	5.60	1.36
0.125	3.2472(3)	5.2159(6)	1.6063	11.4	5.59	1.39
0.150	3.2465(4)	5.2168(7)	1.6069	8.9	5.57	1.41
0.200	3.2457(5)	5.2199(9)	1.6082	7.7	5.54	1.43

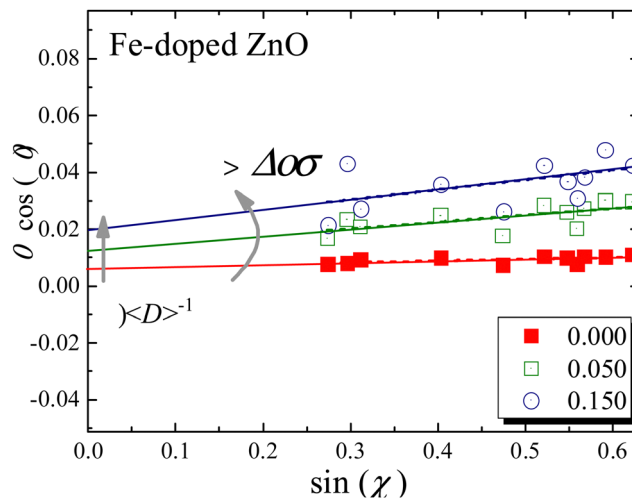


Fig. 3 Williamson-Hall plot for the undoped ($x = 0.000$) and Fe-doped ($x = 0.050, 0.150$) NPs. Solid (red, green, and blue) lines are the best fit of the experimental data using eqn (1).

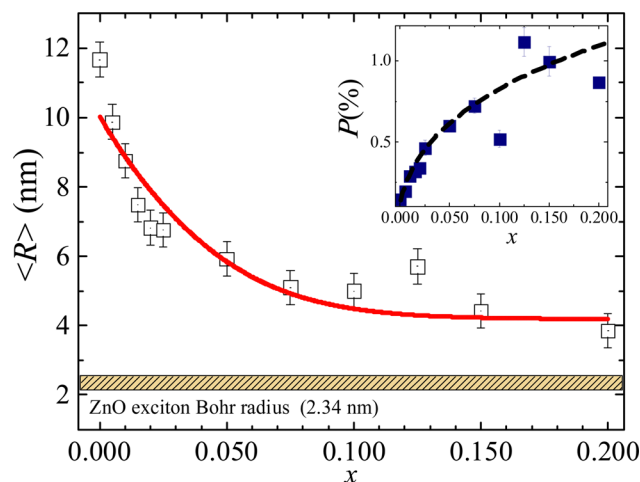


Fig. 4 Crystallite radius as a function of the Fe-content (x). The inset shows the residual strain as a function of the Fe-content (x). Note the ZnO exciton Bohr radius value (2.34 nm) reported in ref. 22. The solid red line is the best fit of the experimental data using eqn (3). The dashed black line in the inset is only a guide to the eye.

value of the undoped sample is 5.68 g cm^{-3} , which is very close to the theoretical value (5.67 g cm^{-3}) for ZnO.¹⁸ However, a monotonic tendency toward lower density values with increasing Fe-content is observed (see Table 1); this tendency is linked to atomic weight losses brought on by the replacement of Zn (65.4 g mol^{-1}) atoms with Fe (55.8 g mol^{-1}) atoms.

To extract the mean crystallite size and residual strain, the corrected linewidths (β) of the Bragg diffraction peaks are correlated to the mean crystallite size ($\langle D \rangle$) and residual strain ($\langle \epsilon \rangle$), through the Williamson-Hall plot (WHP) given by:

$$\beta \cos(\theta) = \frac{K\lambda}{\langle D \rangle} + 4\langle \epsilon \rangle \sin(\theta) \quad (1)$$



where K is a dimensionless factor that depends on the particle shape ($K \sim 0.9$ for spherical shape). If one plots $\beta \cos(\theta)$ as a function of $\sin(\theta)$, the values of $\langle D \rangle$ and $\langle \varepsilon \rangle$ can be estimated from the intercept and slope associated with the linear function fitting, respectively. The WHP for the undoped ($x = 0.000$) and Fe-doped ($x = 0.050, 0.150$) NPs are displayed in Fig. 3, clearly showing that the intercept and slope associated with eqn (1) increase as the Fe-content increases. These findings suggest a decreasing and increasing tendency in the mean crystallite size ($\propto \langle D \rangle^{-1}$) and residual strain ($\propto \langle \varepsilon \rangle$), respectively (see Fig. 4). The decreasing tendency in the mean crystallite size (see Table 1) as the Fe-content increases is in agreement with previous report of Fe-doped ZnO.¹⁹

In the approach of spherical shape NPs the mean crystallite radius ($\langle R \rangle = \langle D \rangle/2$) obtained through the WHP is plotted as a function of the Fe-content (x) in Fig. 4. The observed monotonic decreasing trend of $\langle R \rangle$ versus x (see Fig. 4) could be correlated with a progressive iron-ions enrichment of the NP's surface, decreasing the surface energy in agreement with the Ostwald

ripening equation given by:²⁰

$$\langle R \rangle^3 - \langle R \rangle_0^3 = \frac{8\gamma c_\infty v^2 D}{9R_g T} t \quad (2)$$

where $\langle R \rangle$ is the mean radius, γ is the surface energy per unit area (J m^{-2}), c_∞ is the equilibrium solubility, v is the molar volume of the nanoparticle material, D is the diffusion coefficient, R_g is the ideal gas constant, T is the absolute temperature, and t is the growth time. As it is suggested in the literature, the surface energy could be modeled by the phenomenological equation $\gamma \propto \exp(-Ax)$,²¹ where A is an exponential constant and x is the Fe-content. In this scenario, the crystallite radius can be expressed as:

$$\langle R \rangle^3 = \langle R \rangle_0^3 + k^{-1} \exp(-Ax) \quad (3)$$

where $\langle R \rangle_0$, k and A are fitting parameters. Eqn (3) was used to fit the experimental data as shown in Fig. 4 (see solid red line), giving the following values: $\langle R \rangle_0 = 4.18$ nm, $k = 935.65$ nm³, and $A = 40$. As shown in Fig. 4, there is a strong correlation between the experimental data (open squares) and the model (solid red line).

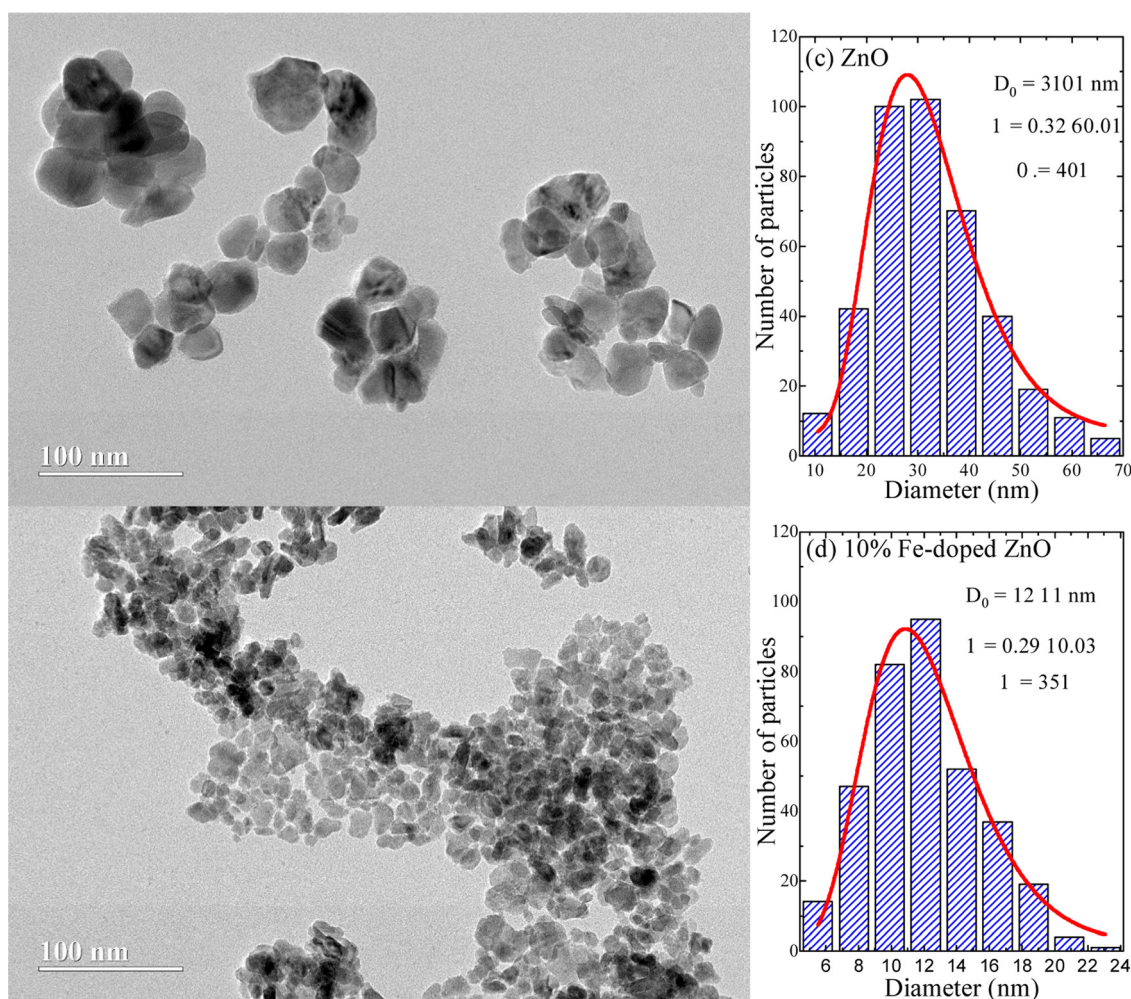


Fig. 5 (a) TEM for the undoped and (b) Fe-doped ZnO nanoparticles, with their corresponding particle size histograms (c) undoped and (d) Fe-doped ZnO. In panels (c) and (d) N means the number of counted particles. The solid lines represent the lognormal fit to each distribution.



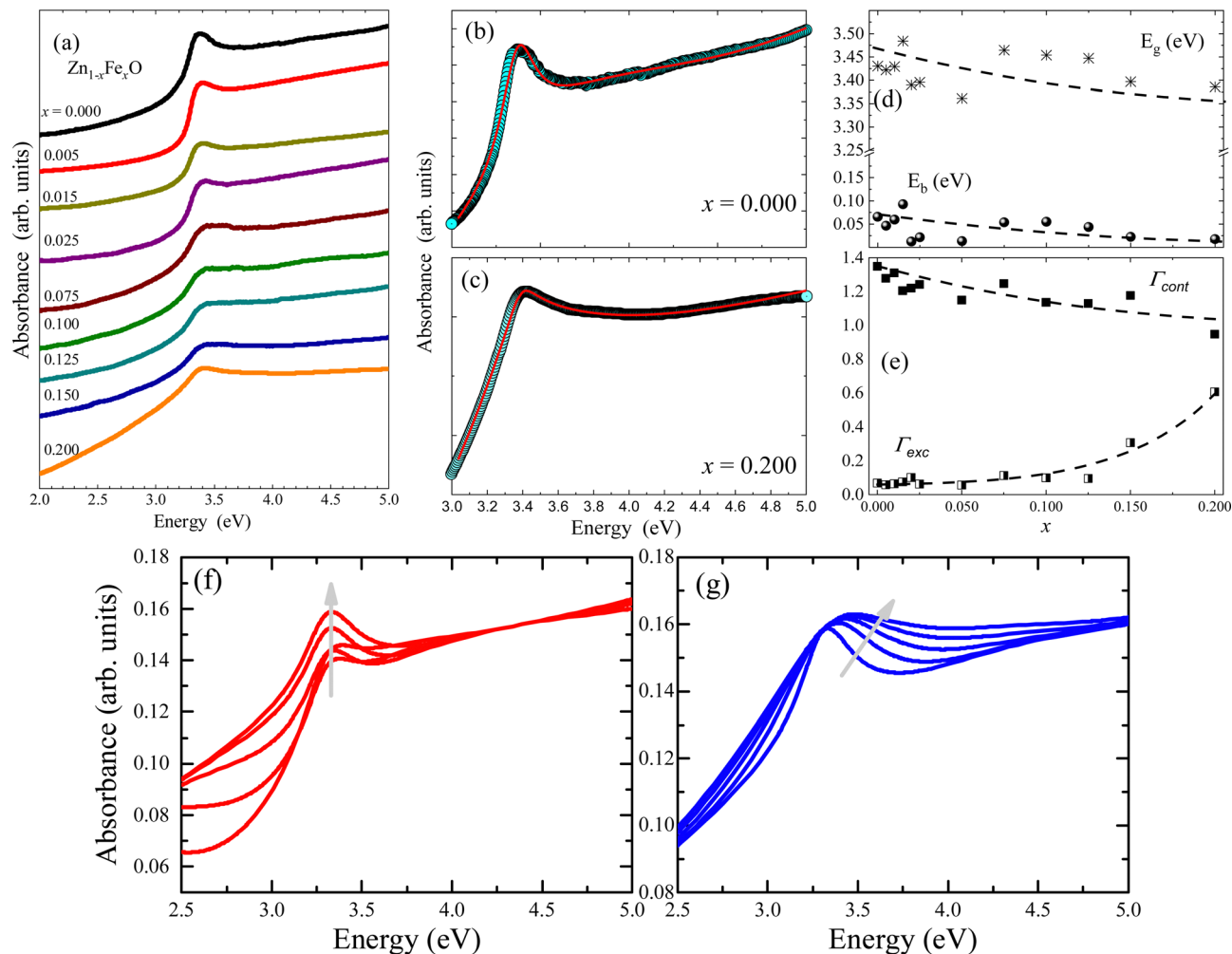


Fig. 6 (a) Absorbance as a function of the optical excitation energy for Fe-undoped ($x = 0.000$) and Fe-doped (from $x = 0.005$ to 0.200) ZnO NPs. (b and c) Experimental data (open symbols) of absorbance versus optical excitation energy and curve fittings (solid red lines) for the ZnO and $\text{Zn}_{0.8}\text{Fe}_{0.2}\text{O}$ NP samples, respectively (curve fit using eqn (4)–(6)). (d) Fitted values of E_g and E_b versus Fe-content (x). (e) Fitted values of Γ_{cont} and Γ_{exc} versus Fe-content (x). Dashed lines in (d) and (e) are guides to the eye. (f and g) Represent theoretical simulations maintaining fix the excitonic (Γ_{exc}) and continuous (Γ_{cont}) broadening parameters, respectively. The gray arrows are guides to the eye.

In addition, the crystallite radii are near the ZnO exciton Bohr radius of 2.34 nm ,²² suggesting that confinement effects can not be ruled out in our samples. Besides, the residual strain (see inset of Fig. 4) shows an increasing trend with progressive iron-doping (x), thus evidencing the rise of micro deformation induced by the entry of iron-ions in the ZnO lattice structure.

Fig. 5(a and b) depict the transmission electron microscopy (TEM) images of undoped and Fe-doped ZnO nanoparticles, respectively. Importantly, the morphological analysis (shape and physical size) of the crystallites shows a clear relationship between crystallite size and Fe-content. The latter suggests that the incorporation of iron ions suppresses the growth of ZnO nanoparticles to a large extent. As previously stated, this is strongly correlated with a progressive iron-ions enrichment of the NP's surface, resulting in a decrease in surface energy. To determine the mean physical size several particles (N) are counted. Fig. 5(c and d) show the histograms, which are curve-fitted using the lognormal distribution function, thus assessing

the mean physical sizes (D_0) of $\sim 31 \pm 1 \text{ nm}$ and $\sim 12 \pm 1 \text{ nm}$, with polydispersity indexes (σ) of 0.32 ± 0.01 and 0.29 ± 0.03 , for the undoped and 10% Fe-doped ZnO, respectively.

The optical properties of undoped and Fe-doped ZnO NPs were assessed using the UV-Visible absorbance as a function of wavelength. For this purpose, powder samples were dispersed in a liquid medium (distilled water) with a concentration of $3 \mu\text{g mL}^{-1}$. Fig. 6 shows the spectra for the undoped ($x = 0.000$) and Fe-doped (x from 0.005 to 0.200) ZnO NPs. As can be seen in Fig. 6, a clear and narrow excitonic peak located in the range of 3.0 – 3.5 eV is observed, which is correlated with the electron-hole pair bound formation. Aiming to determine the exact electronic bandgap and excitonic properties of the as-fabricated materials, Elliot's approach was used to model the absorbance versus energy curves. It is worth mentioning that this approach has been successfully used to analyze other systems, such as perovskites.^{23,24} However, to the best of our knowledge, this is the first time it is used to analyze the $\text{Zn}_{1-x}\text{Fe}_x\text{O}$ system. Elliot's



approach shows that the optical absorption coefficient (α) depends on the linear combination of the exciton (α_{exc}) plus continuous edge (α_{cont}), given by the following relationship:²⁴

$$\alpha = \alpha_{\text{exc}} + \alpha_{\text{cont}} \quad (4)$$

The first contribution in eqn (4) correlates with the exciton formation (electron–hole pair), whereas the second contribution accounts for the absorption into the free-carrier continuum. However, two key aspects need to be included in the description of the samples herein reported and related to the excitonic transitions. Firstly, the NPs size monotonically decreases with the Fe-content, as shown in Fig. 4. Secondly, the entry of the iron ions into the hosting ZnO crystal structure leads to local distortions in the neighboring iron-ions, thus increasing the polydispersity of the exciton peak. In this scenario, the excitonic transition broadening parameter (Γ_{exc}) is included in Elliot's method:

$$\alpha_{\text{exc}} = \alpha_0 \left[\sum_{n=1}^{\infty} \frac{4E_{\text{b}}}{n^3} \left(\frac{\hbar\nu - \left(E_{\text{g}} - \frac{E_{\text{b}}}{n^2} \right)}{\Gamma_{\text{exc}}} \right) \right] \quad (5)$$

where E_{g} and E_{b} are the bandgap and exciton binding energy, respectively. On the other hand, the continuous edge contribution (α_{cont}) is strongly dependent on the free-carrier concentration, which is correlated with the increase of defects associated with the Fe-content increase, causing a flattening of the absorption above the band gap energy. This behavior is phenomenologically modeled using the inverse lognormal distribution function ($f(\hbar\nu)^{-1}$), from which the continuous broadening parameter (Γ_{cont}) is obtained (see eqn (6)). See ref. 24 for

more details about Elliot's approach.

$$\alpha_{\text{cont}}(\hbar\nu) = \alpha_0 \left(\frac{2\hbar\nu}{1 + \exp\left(-2\pi\sqrt{\frac{E_{\text{b}}}{(\hbar\nu - E_{\text{g}})}}\right)} \right) \left(\frac{\hbar\nu - E_{\text{g}}}{f(\hbar\nu)^{-1}} \right). \quad (6)$$

Using eqn (4)–(6), typical fittings of the absorbance regarding the undoped ($x = 0.000$) and Fe-doped ($x = 0.200$) ZnO NPs are displayed in Fig. 6(b and c), respectively. For the undoped ZnO, values of $E_{\text{g}} \sim 3.4$ eV and $E_{\text{b}} \sim 66$ meV were obtained, in very good agreement with the reported values of $E_{\text{g}} \sim 3.37$ eV and $E_{\text{b}} \sim 60$ meV.²⁵ However, as the Fe-content (x) increases, a slight and monotonic reduction trend in both E_{g} and E_{b} is observed, as shown in Fig. 6(d). Concerning the broadening parameters (see Fig. 6(e)), one observes opposite trends as the Fe-content (x) increases. The excitonic transition broadening parameter (Γ_{exc}) increases as the Fe-content increases, very likely evidencing an enhancement of the ZnO matrix disorder. Meanwhile, the continuous broadening parameter (Γ_{cont}) exhibits monotonic reduction as the Fe-content increases, which is associated with the decreasing of the free-carrier concentration, very likely connected with the removal of intrinsic defects. It is worth noting that reduction of free-carrier concentration leads to an increase in the resistivity, as reported in the literature for Fe-doped ZnO thin films.²⁶ To see clearly the effect of the change of the Γ_{exc} and Γ_{cont} in the curves, the theoretical simulation of the absorbance by fixing Γ_{exc} and decreasing progressively Γ_{cont} is presented in Fig. 6(f), while the opposite behavior is addressed in Fig. 6(g) by fixing Γ_{cont} and increasing the Γ_{exc} contribution. It is clear that the continuous or excitonic contribution, prevail over each other depending on the case.



Fig. 7 FTIR spectra of the undoped and Fe-doped ZnO NPs.



In the first, the continuous part loses relevance while the excitonic peak emerges and exhibits its average width almost without variation as Γ_{cont} contribution is decreasing. In the second (Fig. 6(g)), the half-width excitonic peak broadens while the continuous part almost maintains its shape, the Γ_{exc} contribution increases.

Fig. 7 shows the FTIR spectra of the undoped and Fe-doped ZnONPs, all of which exhibit the expected spectra of the ZnO structure.⁵ However, due to neighborhood modifications, iron-ions are located into the core or onto the surface of the ZnO NPs lead to FTIR spectra displaying considerable alterations. Before looking deeper into the details, it is worth noting the band at $\sim 3437 \text{ cm}^{-1}$, observed in all spectra, which can be associated with the O–H stretching mode adsorbed from the environment.²⁷ Moreover, bands at ~ 2922 and $\sim 2852 \text{ cm}^{-1}$ are respectively attributed to asymmetrical and symmetrical C–H stretching vibrations of CH_2 groups.²⁸ Finally, the band at $\sim 1632 \text{ cm}^{-1}$ is attributed to the O–H bending mode.²⁹ It is herein hypothesized that the above-mentioned mode could be adsorbed by the NPs' surface from the reaction medium and by handling the samples in the air atmosphere. On the other hand, the inorganic vibrational frequency of the Zn–O is observed below 700 cm^{-1} , which is specifically located at $\sim 423 \text{ cm}^{-1}$ for the undoped ZnO NPs, slightly below the value ($\sim 431 \text{ cm}^{-1}$) reported in the literature.⁵ Furthermore, an additional vibrational mode, possibly associated with a secondary iron oxide phase has not been observed within the limit of detection of the FTIR equipment (expected for Fe_2O_3 in the range of $578\text{--}567 \text{ cm}^{-1}$ ³⁰). The FTIR observation is in good agreement with the XRD data.

To assess the effect caused by the entry of iron-ions into the ZnO matrix, the shift in the position of the Zn–O band in the FTIR spectra ($400\text{--}700 \text{ cm}^{-1}$) was monitored. In this regard, the spectra were fitted using two Lorentzian peaks, for both undoped and Fe-doped ZnO NPs, revealing for the former ($x = 0.000$) two peaks located at $\sim 423 \text{ cm}^{-1}$ and $\sim 532 \text{ cm}^{-1}$. The main mode shift (below 430 cm^{-1}) is displayed in Fig. 8(a), from where one can see a clear tendency to down shift up to $\sim 7.5\%$, following a gradual increase as the Fe-doping increases. This finding could be related to the possibility of iron entering into the ZnO crystal structure using two different oxidation states, namely Fe^{2+} at lower and Fe^{3+} at higher doping, in agreement with the XRD analysis. The following frequency equation can be used to explain the experimental observation collected in Fig. 8(a):³¹

$$\omega = \frac{1}{2\pi c} \sqrt{\frac{k}{\mu}} \quad (7)$$

where ω represents the FTIR peak frequency, c is the velocity of light, k is the force constant, and μ is the reduced mass for the Zn(Fe)–O bond at a given bond length, given by:

$$\mu = \frac{M_{\text{O}} \times M_{\text{M}}}{(M_{\text{O}} + M_{\text{M}})} \quad (8)$$

In eqn (8) M_{O} is the oxygen mass and M_{M} represents the mass of the metal atom (Zn or Fe). Regarding the force constant



Fig. 8 (a) Zn–O peak position as a function of Fe-content (x) as obtained from the FTIR data. (b) Bond length of the Zn–O extracted from the FTIR data using eqn (7)–(9). (c) Filled blue circles represent the experimental FTIR cubic band intensity ratio $\left(\frac{I_{\text{O-H}}}{I_{\text{Zn-O}}}\right)^3$ as a function of Fe-content, whereas solid red line is the best fit of the data using eqn (3) and (10). Dashed lines in (a) and (b) are guides to the eye.

(k) appearing in eqn (7), it could be expressed by the phenomenological equation proposed by Singh *et al.*³¹

$$k = \frac{B}{l^3} \quad (9)$$

where l is the Zn–O bond length and B is a constant. For bulk ZnO, the estimated value of B is $\sim 10.51 \times 10^{-28} \text{ N m}^2$, which is quite similar to the reported value of B for the Fe–O bond ($17 \times 10^{-28} \text{ N m}^2$).³¹ From these values and using eqn (7)–(9), values of l and k were obtained and collected in Table 2. It is worth noting that the l data collected in Table 2 and extracted from the FTIR data are presented in Fig. 8(b). Moreover, the trend

Table 2 Frequency associated with the Zn–O mode (ω), reduced mass (μ), force constant (k), and bond length (l)

Fe-content (x)	ω (cm^{-1})	μ ($\times 10^{-26}$ Kg)	k (N cm^{-1})	l (\AA)
0.0	423.2	2.1344	1.358	1.9779
1.0	427.1	2.1338	1.383	1.9660
1.5	423.8	2.1335	1.361	1.9764
2.5	419.9	2.1329	1.336	1.9888
5.0	415.1	2.1314	1.305	2.0047
7.5	416.9	2.1298	1.315	1.9992
10.0	421.5	2.1283	1.343	1.9852
12.5	421.9	2.1267	1.345	1.9845
15.0	419.6	2.1251	1.329	1.9922
20.0	425.8	2.1219	1.367	1.9736



displayed in Fig. 8(b) is in very good agreement with the trend obtained from XRD data and presented in Fig. 2(b).

Finally, the FTIR spectra shown in Fig. 7 provide extra information regarding the intensity ratio $\left(\frac{I_{\text{O-H}}}{I_{\text{Zn-O}}}\right)$ of the O-H band and the structural ZnO band. The experimental values (symbols) of the $\left(\frac{I_{\text{O-H}}}{I_{\text{Zn-O}}}\right)^3$ versus the Fe-content (x) are collected in Fig. 8(c), revealing a monotonic and exponential-like increase. This trend can be associated with the increase in surface area due to the monotonic reduction in particle size (see data in Fig. 4). In this scenario, one can suggest the following relationship:

$$\left(\frac{I_{\text{O-H}}}{I_{\text{Zn-O}}}\right)^3 \propto \left(\frac{\text{Surface area}}{\text{Volume}}\right)^3 \propto \frac{1}{\langle R \rangle^3} \quad (10)$$

where $\langle R \rangle$ is the crystallite radius obtained from the XRD analysis and $\frac{1}{\langle R \rangle^3} \propto k \exp(Ax)$. Using eqn (3) into eqn (10) the solid red line in Fig. 8(c) represents the best fit of the experimental data. This finding displays a very good correlation between the XRD and the FTIR data.

The oxidation state of the iron-ions in the doped samples was assessed by room temperature ^{57}Fe Mössbauer spectroscopy. Samples with $x = 0.050$, $x = 0.075$ and $x = 0.200$ were selected for investigation. Fig. 9 shows the recorded spectra of selected samples, with symbols representing the experimental data while the solid red lines represent the best curve fitting using the NORMOS software package. The data analysis provided isomershift (IS) of 0.18 mm s^{-1} for the $x = 0.050$, while slightly increasing for the $x = 0.075$ (IS = 0.20 mm s^{-1}) and $x = 0.200$ (IS = 0.21 mm s^{-1}) samples. Meanwhile, the quadrupole

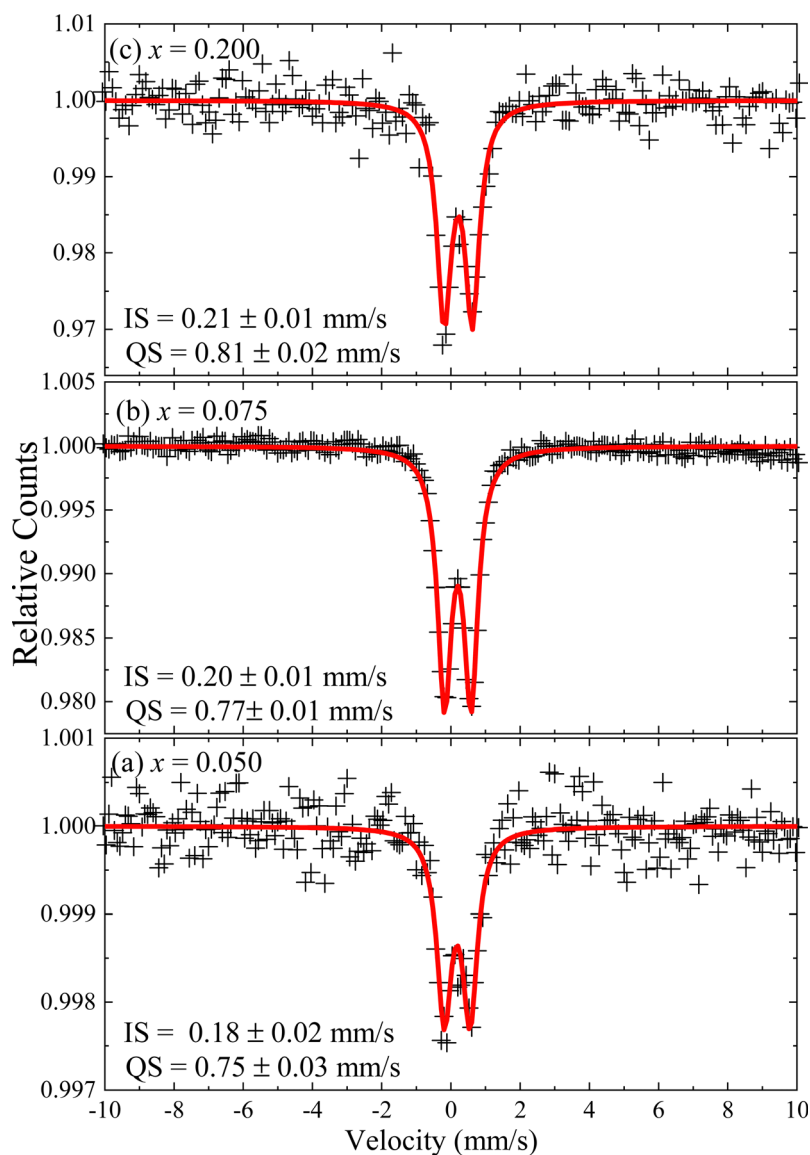


Fig. 9 Room temperature Mössbauer spectra of the Fe-doped ZnO NPs. (a) $x = 0.050$, (b) $x = 0.075$, and (c) $x = 0.200$. Symbols are experimental data and the solid red lines are the best fit of the spectra for one doublet.



splitting (QS) shows a similar trend, slightly increasing from 0.75 mm s^{-1} to 0.81 mm s^{-1} for the $x = 0.050$ and $x = 0.200$ samples, respectively. The obtained hyperfine parameters suggest the presence of Fe^{3+} -ions in the Fe-doped ZnO NPs. However, as reported by Xiao *et al.*,³² the values of the hyperfine parameters (IS = 0.3 mm s^{-1} and QS = 0.83 mm s^{-1}) obtained for Fe-doped (x in the range of 0.010–0.100) ZnO NPs correspond to Fe^{2+} -ions occupying tetrahedral sites (ZnO_4), which was supported by theoretical calculations of the electronic structure in Fe-doped ZnO matrix. Moreover, this result is in agreement with another report of Fe-doped ZnO wurtzite NPs, suggesting the presence of mainly Fe^{2+} -ions and only traces of Fe^{3+} -ions.⁸ As pointed out by Xiao *et al.*,³² it means that the hyperfine parameters of Fe-doped ZnO samples assessed through Mössbauer spectroscopy not directly correlates to the iron oxidation state, as it is the case of unperturbed iron oxide compounds. As Mössbauer spectroscopy directly probes the s -character charge on the nucleus of iron ions, our results suggest charge depletion of Fe^{2+} -ions occupying tetrahedral sites, which is related to the shorter Fe–O bond lengths ($\sim 2.00 \text{ \AA}$) in Fe-doped ZnO NPs with respect to the Fe–O bond length of 2.16 \AA for unperturbed iron oxide compounds.³³ Therefore, reports in the literature support the hypothesis of the presence of Fe^{2+} -ions in the Fe-doped ZnO NPs containing low Fe-content, as suggested by the XRD and FTIR data analysis herein reported. On the other hand, the observed slight increase of the QS as the Fe-content increases could be related to structural disorder increase due to the increase of Fe-content, which can favor the presence of Fe^{3+} -ions, as observed in the samples herein investigated.

In order to assess the magnetic properties of the Fe-doped ZnO NPs magnetic measurements were performed on selected samples (i) at low ($x = 0.005, 0.015, 0.020,$ and 0.025) and (ii) high ($x = 0.100, 0.125,$ and 0.150) Fe-content. Fig. 10(a and b) depict the field dependence of the magnetization (M versus H) recorded at 300 and 2 K. As it is shown in Fig. 10(a), the

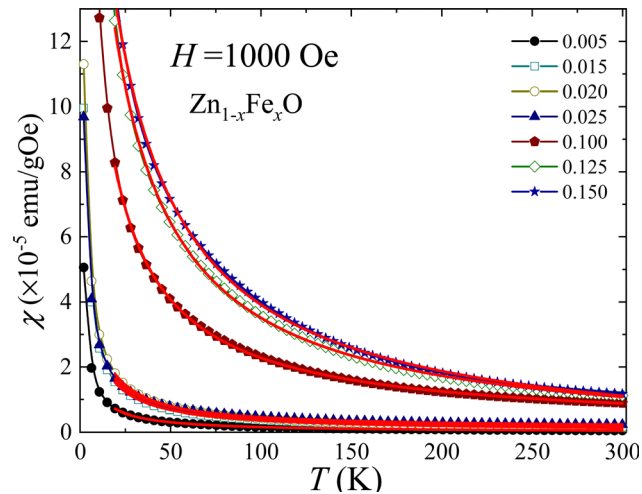


Fig. 11 Temperature dependence of the magnetic susceptibility obtained for selected Fe-doped ZnO NPs. Symbols are experimental data and solid lines are the best fit using eqn (11).

magnetic response at 300 K exhibits paramagnetic behavior, evidenced by a linear behavior with no coercive field ($H_C \sim 0.0 \text{ Oe}$). Differently, the magnetic response at 2 K (see Fig. 10(b)) displays an interesting behavior, with the expected shape of a paramagnetic loop. Data recorded at 2 K show an increasing coercivity (H_C) as the Fe-content increases (see inset of Fig. 10(b)), thus evidencing the increase of the iron ions interaction with the increasing Fe-content. Additionally, the temperature dependence of the magnetic susceptibility (χ) was recorded in the range of 5–300 K while applying a magnetic field of 1 kOe. Fig. 11 displays the χ versus T curves for all selected samples, confirming the dominant paramagnetic behavior, in agreement with the M versus H curves shown in Fig. 10(a and b).

The Curie–Weiss law, given by eqn (11), was used to analyze the χ versus T curves shown in Fig. 10 in the temperature range of 20–300 K, where the Curie–Weiss law is minimally

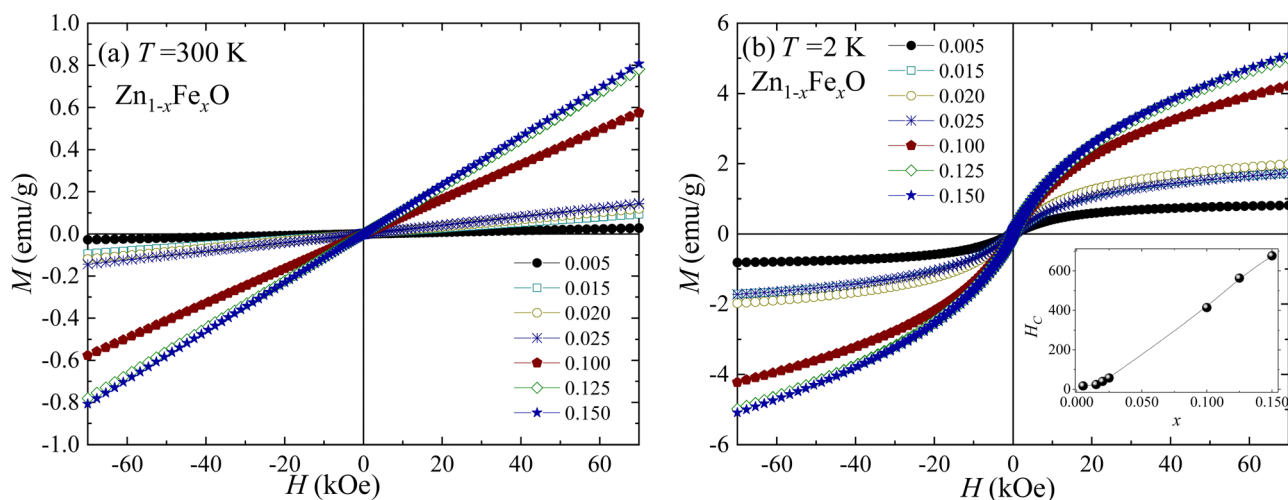


Fig. 10 Magnetization (M) as a function of the magnetic field (H) carried out at (a) 300 K and (b) 2 K for the Fe-doped ZnO NPs. The inset in (b) displays the coercivity (H_C) dependence of the Fe-content.



Table 3 Parameters obtained from the data fit of χ versus T curves (see Fig. 11) of selected Fe-doped samples using the Curie–Weiss law

Fe (x)	C ($\times 10^{-5}$ emu K g $^{-1}$ Oe $^{-1}$)	θ_{CW} (K)	χ_0 ($\times 10^{-7}$ emu g $^{-1}$ Oe $^{-1}$)	μ_{eff} (μ_{B})
0.005	16.7	−4.03	0.002	5.10
0.015	36.0	−4.65	2.099	4.32
0.020	43.1	−5.05	1.317	4.10
0.025	35.7	−4.23	11.72	3.33
0.100	242.0	−10.7	10.14	4.32
0.125	443.0	−15.6	−32.61	5.21
0.150	533.0	−19.0	−55.91	5.22

influenced by Fe–Fe interactions.

$$\chi = \chi_0 + \frac{C}{T - \theta_{\text{CW}}} \quad (11)$$

where C is the Curie constant, θ_{CW} is the Curie–Weiss temperature and χ_0 is the temperature-independent magnetic susceptibility.³⁴ The obtained parameters are listed in Table 3.

From the Curie–Weiss law (see eqn (11)) the effective magnetic moment (μ_{eff}) was obtained for all samples. The expected values for the spin-only contribution of free Fe $^{3+}$ -ions and Fe $^{2+}$ -ions are $5.9\mu_{\text{B}}$ and $5.2\mu_{\text{B}}$, respectively. As shown in Table 3, the obtained value of $\mu_{\text{eff}} = 5.10\mu_{\text{B}}$ for $x = 0.005$ is very much close to the expected value for Fe $^{2+}$ -ions, suggesting the presence of Fe $^{2+}$ -ions at lower Fe-content, in good agreement with the XRD and FTIR assessed data. Meanwhile, the μ_{eff} value decreases as the Fe-content increases up to $x = 0.025$. However, in the higher end of Fe-content ($x = 0.100, 0.125,$ and 0.150) the effective magnetic moment (μ_{eff}) increases, suggesting the onset of Fe $^{3+}$ -ions. Moreover, in the higher end of Fe-content, θ_{CW} shows negative and increasing values (see Table 3) as the Fe-content increases, suggesting the occurrence of a short-range antiferromagnetic (AFM) correlation between iron spins ($\uparrow\downarrow\cdots\uparrow\downarrow$) dispersed in the hosting matrix. The onset of this AFM interaction is claimed to be responsible for the observed discrepancies between the effective magnetic moment (see Table 3) and the value for free Fe $^{3+}$ -ions. A similar behavior was reported for Fe-doped ITO.³⁵

4. Conclusions

The present study reports on the successful synthesis of single phase Fe-doped ZnO samples presenting the wurtzite structure. The structural characterization, assessed by XRD measurements, reveals a major effect of iron-ion entry into the ZnO matrix, namely a decreasing tendency of crystallite size with increasing Fe-content. This behavior was modeled using the Ostwald ripening equation plus a phenomenological dependence of the surface energy with Fe-content. Moreover, the crystallite radii values are close to the ZnO exciton Bohr radius (2.34 nm), asymptotically approaching this value as the Fe-content increases. Additionally, UV-Vis characterization reveals an excitonic peak associated with both the band gap energy (E_{g}) and binding energy (E_{b}). Values of E_{g} and E_{b} were extracted from the absorbance data by modeling the absorption

coefficient using a combination of excitonic peak plus continuous edge, through a modified Elliot's approach including an inverse lognormal distribution function. The FTIR measurements proved to be a valuable tool for determining the structural properties of Fe-doped ZnO, which is consistent with the change in bond length and increase in the surface area suggested by XRD data. Finally, our results show strong evidence of the entry of Fe $^{2+}$ -ions as a solid solution with Zn $^{2+}$ -ions at low Fe-content, whereas for high Fe-content the coexistence of Fe $^{3+}$ /Fe $^{2+}$ is increased, in agreement with magnetic measurements.

Conflicts of interest

There are no conflicts to declare.

Acknowledgements

This research work was carried out with the financial support of the UNSA INVESTIGA (Grant No. IBA-IB-13-2020-UNSA). The LVL author thanks to CAPES for the postdoctoral fellowship (No. 88887.319028/2019-00).

References

- M. L. Dinesha, G. D. Prasanna, C. S. Naveen and H. S. Jayanna, Structural and dielectric properties of Fe doped ZnO nanoparticles, *Indian J. Phys.*, 2013, **87**, 147–153.
- M. A. Ciciliati, M. F. Silva, D. M. Fernandes, M. A. C. de Melo, A. A. W. Hechenleitner and E. A. G. Pineda, Fe-doped ZnO nanoparticles: Synthesis by a modified sol–gel method and characterization, *Mater. Lett.*, 2015, **159**, 84–86.
- E. Rokhsat and A. Khayatian, Enhanced photocatalytic activity of Fe doped ZnO hierarchical nanosheets on the degradation of p-nitrophenol under visible light, *Inorg. Nano-Met. Chem.*, 2018, **48**, 203–209.
- L. Dimesso, Pechini Processes: An Alternate Approach of the Sol–Gel Method, Preparation, Properties, and Applications, in *Handbook of Sol-Gel Science and Technology*, ed. L. Klein, M. Aparicio and A. Jitianu, Springer, Cham, 2016, pp. 1–22, DOI: [10.1007/978-3-319-19454-7_123-1](https://doi.org/10.1007/978-3-319-19454-7_123-1).
- S. C. Andia-Huaracha, L. M. Zapana-Cayo, F. F. H. Aragón, J. C. R. Aquino, J. A. H. Coaquira, C. D. Gonzales-Lorenzo, J. S. Ayala-Arenas, J. L. Solis, P. C. Morais and D. G. Pacheco-Salazar, Tuning the photocatalytic activity of ZnO nanoparticles by the annihilation of intrinsic defects provoked by the thermal annealing, *J. Nanopart. Res.*, 2022, **24**, 50.
- P. R. Sharma, S. K. Sharma, R. Antoine and B. S. Hsiao, Efficient Removal of Arsenic Using Zinc Oxide Nanocrystal-Decorated Regenerated Microfibrillated Cellulose Scaffolds, *ACS Sustainable Chem. Eng.*, 2019, **7**, 6140–6151.
- R. Wang, A. W. Sleight and M. A. Subramanian, An Unusual Iron Site in Iron-Doped Zinc Oxide, *J. Solid State Chem.*, 1996, **125**, 224–227.
- J. Xiao, A. Kuc, S. Pokhrel, M. Schowalter, S. Parlapalli, A. Rosenauer, T. Frauenheim, L. Mädler, L. G. M. Pettersson



- and T. Heine, Evidence for Fe²⁺ in Wurtzite Coordination: Iron Doping Stabilizes ZnO Nanoparticles, *Small*, 2011, **7**, 2879–2886.
- 9 S. George, S. Pokhrel, T. Xia, B. Gilbert, Z. Ji, M. Schowalter, A. Rosenauer, R. Damoiseaux, K. A. Bradley, L. Mädler and A. E. Nel, Use of a Rapid Cytotoxicity Screening Approach To Engineer a Safer Zinc Oxide Nanoparticle through Iron Doping, *ACS Nano*, 2010, **4**, 15–29.
 - 10 P. S. Miedema and F. M. F. de Groot, The iron L edges: Fe 2p X-ray absorption and electron energy loss spectroscopy, *J. Electron Spectrosc. Relat. Phenom.*, 2013, **187**, 32–48.
 - 11 J. T. Luo, Y. C. Yang, X. Y. Zhu, G. Chen, F. Zeng and F. Pan, Enhanced electromechanical response of Fe-doped ZnO films by modulating the chemical state and ionic size of the Fe dopant, *Phys. Rev. B: Condens. Matter Mater. Phys.*, 2010, **82**, 014116.
 - 12 B. Toby, EXPGUI, a graphical user interface for GSAS, *J. Appl. Crystallogr.*, 2001, **34**, 210–213.
 - 13 A. Galdámez-Martínez, G. Santana, F. Güell, P. R. Martínez-Alanis and A. Dutt, Photoluminescence of ZnO Nanowires: A Review, *Nanomaterials*, 2020, **10**, 857.
 - 14 R. D. Shannon, Revised effective ionic radii and systematic studies of interatomic distances in halides and chalcogenides, *Acta Crystallogr., Sect. A: Cryst. Phys., Diffr., Theor. Gen. Crystallogr.*, 1976, **32**, 751–767.
 - 15 R. H. R. Castro, P. Hidalgo, J. A. H. Coaquira, J. Bettini, D. Zanchet and D. Gouvêa, Surface Segregation in SnO₂–Fe₂O₃ Nanopowders and Effects in Mössbauer Spectroscopy, *Eur. J. Inorg. Chem.*, 2005, 2134–2138.
 - 16 T. Kataoka, M. Kobayashi, Y. Sakamoto, G. S. Song, A. Fujimori, F.-H. Chang, H.-J. Lin, D. J. Huang, C. T. Chen, T. Ohkochi, Y. Takeda, T. Okane, Y. Saitoh, H. Yamagami, A. Tanaka, S. K. Mandal, T. K. Nath, D. Karmakar and I. Dasgupta, Electronic structure and magnetism of the diluted magnetic semiconductor Fe-doped ZnO nanoparticles, *J. Appl. Phys.*, 2010, **107**, 033718.
 - 17 J. A. McLeod, D. W. Boukhvalov, D. A. Zatsépin, R. J. Green, B. Leedahl, L. Cui, E. Z. Kurmaev, I. S. Zhidkov, L. D. Finkelstein, N. V. Gavrilov, S. O. Cholakh and A. Moewes, Local Structure of Fe Impurity Atoms in ZnO: Bulk versus Surface, *J. Phys. Chem. C*, 2014, **118**, 5336–5345.
 - 18 S. C. Abrahams and J. L. Bernstein, Remeasurement of the structure of hexagonal ZnO, *Acta Crystallogr., Sect. B: Struct. Crystallogr. Cryst. Chem.*, 1969, **25**, 1233–1236.
 - 19 Y. Cherifi, A. Chaouchi, Y. Lorgouilloux, M. Rguiti, A. Kadri and C. Courtois, Electrical, dielectric and photocatalytic properties of Fe-doped ZnO nanomaterials synthesized by sol gel method, *Process. Appl. Ceram.*, 2016, **10**, 125–135.
 - 20 A. Baldan, Review Progress in Ostwald ripening theories and their applications to the γ' -precipitates in nickel-base superalloys Part II Nickel-base superalloys, *J. Mater. Sci.*, 2002, **37**, 2379–2405.
 - 21 D. G. Pacheco-Salazar, F. F. H. Aragón, L. Villegas-Lelovsky, A. Ortiz de Zevallos, G. E. Marques and J. A. H. Coaquira, Engineering of the band gap induced by Ce surface enrichment in Ce-doped SnO₂ nanocrystals, *Appl. Surf. Sci.*, 2020, **527**, 146794.
 - 22 R. T. Senger and K. K. Bajaj, Optical properties of confined polaronic excitons in spherical ionic quantum dots, *Phys. Rev. B: Condens. Matter Mater. Phys.*, 2003, **68**, 045313.
 - 23 Y. Yang, M. Yang, K. Zhu, J. C. Johnson, J. J. Berry, J. van de Lagemaat and M. C. Beard, Large polarization-dependent exciton optical Stark effect in lead iodide perovskites, *Nat. Commun.*, 2016, **7**, 12613.
 - 24 S. Neutzner, F. Thouin, D. Cortecchia, A. Petrozza, C. Silva and A. R. SrimathKandada, Exciton-polaron spectral structures in two-dimensional hybrid lead-halide perovskites, *Phys. Rev. Mater.*, 2018, **2**, 064605.
 - 25 N. Kamarulzaman, M. F. Kasim and R. Rusdi, Band Gap Narrowing and Widening of ZnO Nanostructures and Doped Materials, *Nanoscale Res. Lett.*, 2015, **10**, 346.
 - 26 P. L. Hadimani, S. S. Ghosh and A. Sil, Preparation of Fe doped ZnO thin films and their structural, magnetic, electrical characterization, *Superlattices Microstruct.*, 2018, **120**, 199–208.
 - 27 G. Rytwo, R. Zakai and B. Wicklein, The Use of ATR-FTIR Spectroscopy for Quantification of Adsorbed Compounds, *J. Spectrosc.*, 2015, **2015**, 727595.
 - 28 J. Y. Chen, H. Zhang, J. Ma, T. Tuchiya and Y. Miao, Determination of the degree of degradation of frying rapeseed oil using Fourier-transform infrared spectroscopy combined with partial least-squares regression, *Int. J. Anal. Chem.*, 2015, **2015**, 185367.
 - 29 H. Sanaeishoar, M. Sabbaghan and F. Mohave, Synthesis and characterization of micro-mesoporous MCM-41 using various ionic liquids as co-templates, *Microporous Mesoporous Mater.*, 2015, **217**, 219–224.
 - 30 Y. Wang, A. Muramatsu and T. Sugimoto, FTIR analysis of well-defined α -Fe₂O₃ particles, *Colloids Surf., A*, 1998, **134**, 281–297.
 - 31 H. Singh and K. L. Yadav, Structural, dielectric, vibrational and magnetic properties of Sm doped BiFeO₃ multiferroic ceramics prepared by a rapid liquid phase sintering method, *Ceram. Int.*, 2015, **41**, 9285–9295.
 - 32 J. Xiao, A. Kuc, S. Pokhrel, L. Mädler, R. Pöttgen, F. Winter, T. Frauenheim and T. Heine, Fe-Doped ZnO Nanoparticles: The Oxidation Number and Local Charge on Iron, Studied by 57Fe Mössbauer Spectroscopy and DFT Calculations, *Chem. – Eur. J.*, 2013, **19**, 3287–3291.
 - 33 H. Fjellvåg, F. Grønvold, S. Stølen and B. Hauback, On the Crystallographic and Magnetic Structures of Nearly Stoichiometric Iron Monoxide, *J. Solid State Chem.*, 1996, **124**, 52–57.
 - 34 K. Das, I. Ahmedmir, R. Ranjan and H. B. Bohidar, Size-dependent magnetic properties of cubic-phase MnSe nanospheres emitting blue-violet fluorescence, *Mater. Res. Express*, 2018, **5**, 056106.
 - 35 F. F. H. Aragón, J. A. H. Coaquira, S. W. da Silva, R. Cohen, D. G. Pacheco-Salazar and L. C. C. M. Nagamine, Fe content effects on structural, electrical and magnetic properties of Fe-doped ITO polycrystalline powders, *J. Alloys Compd.*, 2021, **867**, 158866.

